J Adv Ceram

Research Article

Regulation of the sintering trajectory of Ho,Pr:Y_2O_3 ceramics for 2.9 μm mid-infrared lasers by atmospheric sintering

Qing Li[1,2], Fei Liang[1], Jun Wang[2,✉], Yan Ling Xue[3,4,5,✉], Jie Ma[2], Peng Liu[2], Shiyu Sun[6], Zhan Hui[3], Jian Zhang[7], Changhua Zhang[8], Lili Hu[6], Haohai Yu[1], Huaijin Zhang[1], Dingyuan Tang[8,✉]

Cite this article: Li Q, Liang F, Wang J, et al. *J Adv Ceram* 2025, **14**(1): 9221006. https://doi.org/10.26599/JAC.2024.9221006

ABSTRACT: The sintering trajectory of the Ho,Pr:Y_2O_3 ceramics could be effectively adjusted by sintering in a flowing oxygen atmosphere instead of vacuum. The final-stage grain growth was significantly suppressed by the use of oxygen atmosphere presintering, resulting in smaller average grain sizes than those of samples sintered under vacuum, while the same relative density was achieved. After hot isostatic pressing (HIP), the oxygen presintered Ho,Pr:Y_2O_3 ceramics achieved excellent optical quality, with transmittance exceeding 80% at a wavelength of 680 nm. The codoping of Pr^{3+} as deactivating ions effectively depopulated the lower energy level $^5I_7$ during the Ho^{3+}:$^5I_6 \rightarrow {}^5I_7$ transition, thereby making the Ho,Pr:Y_2O_3 ceramics more conducive to promoting population inversion in the 2.9 μm laser wavelength range.

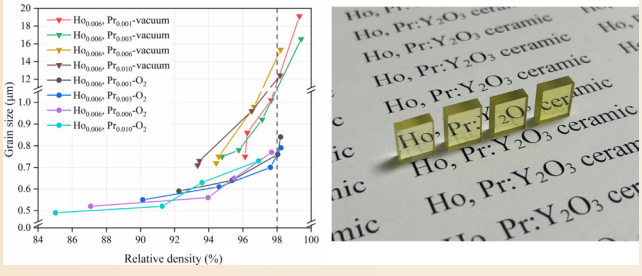

KEYWORDS: Y_2O_3 ceramics; sintering trajectory; Ho^{3+}/Pr^{3+}; mid-infrared laser; fluorescence properties

1 Introduction

Mid-infrared laser sources operating at 2.7–3 μm have significant applications in remote sensing, directional IR countermeasures, medical surgery, etc., because emissions in this spectral region are located in the atmospheric transmission window, and strong absorption by water molecules enables the availability of laser scalpels for high-precision treatment [1–4]. These lasers also serve as pump sources for optical parametric oscillators to achieve laser outputs with extended wavelengths [5,6]. Ho^{3+}-doped laser materials emitting at 2.9 μm are of particular interest because of their ability to generate short pulsed lasers and allow flexible wavelength modulation [7–9]. However, the much shorter fluorescence lifetime of the upper laser level ($^5I_6$) than of the lower laser level ($^5I_7$) tends to induce a self-termination effect that hampers population inversion [10,11]. Fortunately, codoping with Pr^{3+} ions can effectively depopulate the Ho^{3+}:$^5I_7$ level through energy transfer to the Pr^{3+}:$^3F_2$ level, as demonstrated in various materials, such as Ho, Pr codoped $LiLuF_4$, $LiYF_4$, CaF_2, $Gd_2YSc_2Ga_3O_{12}$, $YAlO_3$ (YAP) crystals [3,8,11–16], and ZBLAN fibers [17,18].

Yttrium oxide (Y_2O_3), with a low phonon energy of 560 cm^{-1} and a high thermal conductivity of 13.4 W/(m·K), is a promising host material for mid-infrared solid-state lasers [19,20]. Currently, Y_2O_3 transparent ceramics have competitive advantages over their conventionally grown single-crystal counterparts, such as volume scalability, designed structure and high doping concentration [21]. To meet the requirements of laser applications, these ceramics must have low scattering loss and high optical uniformity, requiring residual pores to be minimized below 0.0001% [22]. However, during the final-stage sintering of sesquioxide ceramics, an increase in relative density is often accompanied by a high grain boundary migration rate, leading to pore-boundary separation. For example, Serivalsatit and Ballato [23] reported that inappropriate control over the sintering procedure of Er:Sc_2O_3 ceramics could lead to the formation of intragranular pores within some grains, even though the average grain size had reached less than 1 μm. While employing a two-step sintering technique to minimize the average grain size to the greatest extent, eliminating the intragranular pores and greatly improving the transmittance of Er:Sc_2O_3 ceramics became feasible. This implies the importance

[1] State Key Laboratory of Crystal Materials and Institute of Crystal Materials, Shandong University, Jinan 250100, China. [2] Jiangsu Key Laboratory of Advanced Laser Materials and Devices, School of Physics and Electronic Engineering, Jiangsu Normal University, Xuzhou 221116, China. [3] Shanghai Key Laboratory of Multidimensional Information Processing, School of Communication and Electronics Engineering, East China Normal University, Shanghai 200241, China. [4] Shanghai Branch, Hefei National Laboratory, and Shanghai Research Center for Quantum Sciences, Shanghai 201315, China. [5] Collaborative Innovation Center of Extreme Optics, Shanxi University, Taiyuan 030006, China. [6] Shanghai Institute of Optics and Fine Mechanics, Chinese Academy of Sciences, Shanghai 201800, China. [7] Shanghai Institute of Ceramics, Chinese Academy of Sciences, Shanghai 201899, China. [8] Future Technology School, Shenzhen Technology University, Shenzhen 518118, China.

✉ Corresponding authors. E-mail: J. Wang, jwang025@e.ntu.edu.sg; Y. Xue, ylxue@ee.ecnu.edu.cn; D. Tang, tangdingyuan@sztu.edu.cn

Received: July 9, 2024; Revised: November 11, 2024; Accepted: November 20, 2024

of achieving a high sintered density with minimal grain growth during the final stage of sintering.

Traditionally, the grain boundary migration rate of Y_2O_3 ceramics can be suppressed by doping with tetravalent cations (M^{4+}, M = Zr, Th, Hf, etc.) [24–28]. This is because the diffusion rate of Y^{3+} cations in Y_2O_3 is significantly lower than that of O^{2-} anions, making the grain boundary mobility of Y_2O_3 ceramics primarily determined by the diffusion of Y^{3+} cations. The incorporation of M^{4+} cations into Y_2O_3 ceramics can effectively reduce the concentrations of Y^{3+} interstitials, thereby decreasing the grain growth rate [24,29]. Nevertheless, this introduces lattice point defects due to the charge imbalance between M^{4+} and host cations (Y^{3+}), leading to photodarkening under high-power laser excitation [30,31]. This results in severe degradation of the laser efficiency and output power. Another effective strategy involves the use of vacuum presintering combined with HIP to regulate the sintering trajectory. Vacuum presintering is employed to achieve an initial density of 95%–99%, followed by HIP to achieve final densification, ensuring that the ceramic's grain size remains consistent, typically below 5 μm. This approach is the current mainstream method for preparing Y_2O_3 transparent ceramics [32–36].

During the sintering of Y_2O_3 ceramics under high oxygen partial pressure, there is an increase in the concentration of oxygen interstitials accompanied by a reduction in cation interstitials. In addition, the valence states of Pr ions in oxides are sensitive to the oxygen partial pressure at high temperatures [37–39]. In this case, the cation defects and the grain boundary mobility of the Pr-doped Ho:Y_2O_3 ceramics might be adjusted by manipulating the sintering atmosphere. In this work, the effects of vacuum presintering and oxygen presintering on the grain growth and densification process of Ho,Pr:Y_2O_3 ceramics were compared. Through oxygen presintering combined with the HIP method, Ho,Pr:Y_2O_3 ceramics with high optical quality were successfully fabricated. The emission spectra and luminescence decays monitored at the Ho^{3+}:$^5I_6 \rightarrow {}^5I_7$ and $^5I_7 \rightarrow {}^5I_8$ transitions were analyzed, and the deactivation effect on the Ho^{3+}:$^5I_7$ level resulting from codoping of Pr^{3+} was discussed.

2 Experimental

2.1 Ceramic fabrication

Commercial Y_2O_3 (purity ≥ 99.99%, Jiahua Advanced Material Resources Co., Ltd., China) and Pr_6O_{11} (purity ≥ 99.99%, Rarechem. Co., Ltd., China) powders were used as the starting materials and dissolved in dilute nitric acid solution. $Ho(NO_3)_3$, $Y(NO_3)_3$, and $Pr(NO_3)_3$ solutions were mixed according to the chemical composition of $(Ho_{0.006}Pr_xY_{0.994-x})_2O_3$ (x = 0.001, 0.003, 0.006, and 0.01) to prepare the mother solution and then diluted with deionized water when the Y^{3+} concentration reached 0.2 mol/L. The precipitate, mixed with NH_4HCO_3 (2 mol/L) and NH_4OH (1.5 mol/L) solutions, was sprayed into the mother solution at a rate of 6 mL/min until the pH reached 8. The detailed spraying system has been reported in the author's previous paper [40]. After aging for approximately 10 h, the precipitate was filtered and washed with deionized water and ethanol to remove the byproducts. After drying at 60 °C for 48 h and then crushing, the precursors were calcined at 1250 °C for 5 h to obtain Ho,Pr:Y_2O_3 powders. Afterwards, the powders were further planetary ball milled for 15 h at 140 r/min, mixed with ZrO_2 balls and ethanol as ball-milling media, and the slurry concentration was approximately 11 vol%. The slurries were subsequently dried, crushed and sieved through a 140 mesh 3 times. The obtained powders were uniaxial pressed into disks of different sizes under a pressure of ~10 MPa and then cold isostatic pressed at 200 MPa. The compacts were either vacuum presintered or oxygen presintered at 1420–1520 °C for 7 h, and further subjected to HIP at 1450 °C for 3 h under 200 MPa argon (Ar) gas, with an average diameter shrinkage of approximately 28% compared with the diameter of the stainless steel mold. Finally, the Ho,Pr:Y_2O_3 ceramics were annealed in a 5% H_2/95% Ar atmosphere at 1000 °C for 10 h and then mirror polished on both surfaces.

2.2 Characterizations

The surface microstructures of the samples were observed by scanning electron microscopy (SEM; JSM-6510, JEOL, Japan), and before observation, the fractures or surfaces of the samples were thermally etched at 1300 °C for 5 h in a muffle furnace. The relative densities of the samples were determined via the Archimedes method. The sizes of at least 200 grains of the samples were measured via a statistical method with Nano Measure software. The phase structures of the samples were identified via an X-ray diffractometer (XRD; Bruker D2, Germany). Absorption spectra and transmittance spectra were measured via a UV-VIS-NIR spectrophotometer (Lambda 950, Perkin-Elmer, USA), and the thickness of the samples for measurement was 3 mm. The fluorescence spectra and luminescence decay curves were measured via a spectrophotometer (FLS 1000, Edinburgh Instruments, UK) under excitation at 640 nm.

3 Results and discussion

Figure 1 compares the sintering trajectories of the Ho,Pr:Y_2O_3 ceramics presintered under vacuum and in a flowing oxygen atmosphere, with sintering temperatures ranging from 1420 to 1520 °C for 7 h. As shown in Fig. 1, the grain size of the Y_2O_3 ceramics sintered under vacuum increased rapidly with increasing relative density. In comparison, the Ho,Pr:Y_2O_3 ceramics sintered in an oxygen atmosphere exhibited slower grain growth as the relative density increased. For example, at approximately 98% relative density (marked by a dashed line in Fig. 1), the samples sintered in an oxygen atmosphere had notably smaller grain sizes than those sintered under vacuum. Generally, the slower velocity of the grain boundaries in Y_2O_3 is more conducive to suppressing the formation of intragranular pores. Consequently, oxygen atmosphere sintering was more effective for controlling the grain boundary mobility and achieving ultimate densification in the Ho,Pr:Y_2O_3 ceramics.

Figure 2 shows the thermally etched surfaces of the Ho,Pr:Y_2O_3

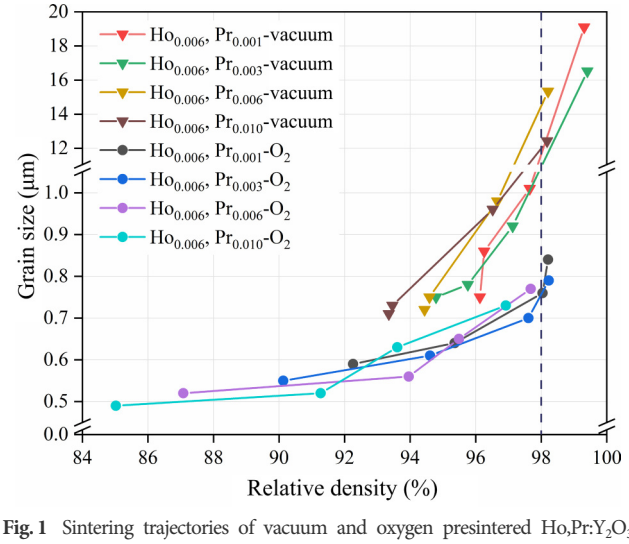

Fig. 1 Sintering trajectories of vacuum and oxygen presintered Ho,Pr:Y_2O_3 ceramics at temperatures of 1420, 1460, 1480, and 1520 °C for 7 h.

ceramics sintered in different atmospheres at 1420 °C for 7 h. At the same Pr doping concentration, the oxygen-sintered Ho,Pr:Y_2O_3 ceramics had smaller grain sizes but higher porosity than those sintered under vacuum, indicating slower densification and grain growth rates. Increasing the sintering temperature to 1520 °C resulted in abnormal grain growth in all vacuum-sintered Ho,Pr:Y_2O_3 ceramics, as shown in Figs. 3(a)–3(d). Pores detached from triple junctions or became entrapped within grains (highlighted by red circles). In contrast, the average grain size of the ceramics sintered in an oxygen atmosphere was less than 0.8 μm, without exaggerated grain growth or intragranular pores (Figs. 3(e)–3(h)). Therefore, presintering the Ho,Pr:Y_2O_3 ceramics in an oxygen atmosphere effectively reduced the grain boundary migration rate and prevented pore-boundary separation during final-stage sintering.

To clearly compare the sintering behaviors of the oxygen-sintered and vacuum-sintered Ho,Pr:Y_2O_3 ceramics, Figs. 4(a)–4(d) illustrate the variations in the grain size and relative density with respect to the sintering temperature for these ceramics in different atmospheres. These figures confirmed that Ho,Pr:Y_2O_3 ceramics sintered in an oxygen atmosphere had slower grain growth and densification rates than those sintered under vacuum. This phenomenon can be explained by Eqs. (1)–(3) [24]. Sintering in a reducing atmosphere, such as vacuum sintering, promotes the generation of oxygen vacancies ($V_O^{\cdot\cdot}$) along with free electrons (e'), whereas an oxygen-enriched environment facilitates the introduction of oxygen interstitials (O_i'') and electron holes ($\dot{h}$). Consequently, the concentration of yttrium interstitials ($Y_i^{\cdot\cdot\cdot}$) in Y_2O_3 is reduced during oxygen atmosphere sintering, which serves as the rate-controlling species controlling grain boundary diffusion and mobility.

Oxygen defect reaction under vacuum sintering (Eq. (1)):

$$O_O \rightarrow V_O^{\cdot\cdot} + 2e' + \frac{1}{2}O_2 \tag{1}$$

Oxygen defect reaction under oxygen sintering (Eq. (2)):

$$\frac{1}{2}O_2 \rightarrow O_i'' + 2\dot{h} \tag{2}$$

Yttrium cation defect reaction (Eq. (3)):

$$[Y_i^{\cdot\cdot\cdot}] = [V_O^{\cdot\cdot}]^{1.5}\left(\frac{K_F}{K_s^{0.5}}\right)\exp\left(-\frac{\Delta G_F - \Delta G_S/2}{kT}\right) = \left[O_i''\right]^{-1.5}\left(\frac{K_F K_F^{A\,1.5}}{K_s^{0.5}}\right)\exp\left(-\frac{\Delta G_F - \Delta G_S/2 + 3\Delta G_F^A/2}{kT}\right) \tag{3}$$

where K_F/K_S is the preexponential constant for Frenkel/Schottky defect reaction, $\Delta G_F/\Delta G_S$ is the Gibbs free energy for Frenkel/Schottky defect formation, the superscripts (A) for K_F^A and G_F^A refer to anion ions, k is the Boltzmann constant, and T is the absolute temperature.

According to Eqs. (4) and (5), some Pr ions are converted to a tetravalent state during sintering in an oxidizing atmosphere. When Pr^{4+} ions substituted Y^{3+} lattice sites, the concentration of

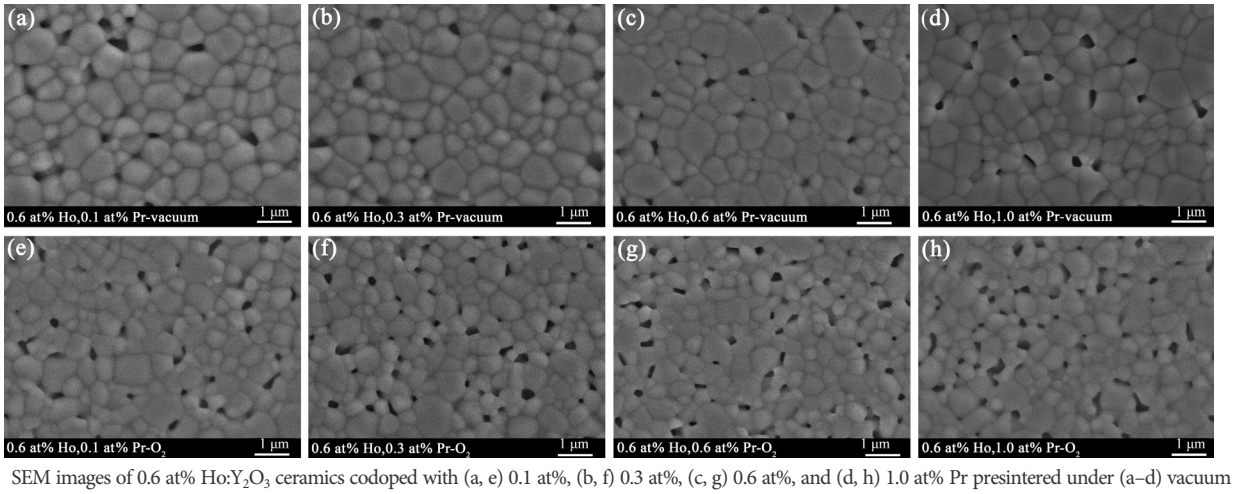

Fig. 2 SEM images of 0.6 at% Ho:Y_2O_3 ceramics codoped with (a, e) 0.1 at%, (b, f) 0.3 at%, (c, g) 0.6 at%, and (d, h) 1.0 at% Pr presintered under (a–d) vacuum and (e–h) flowing oxygen atmosphere at 1420 °C for 7 h.

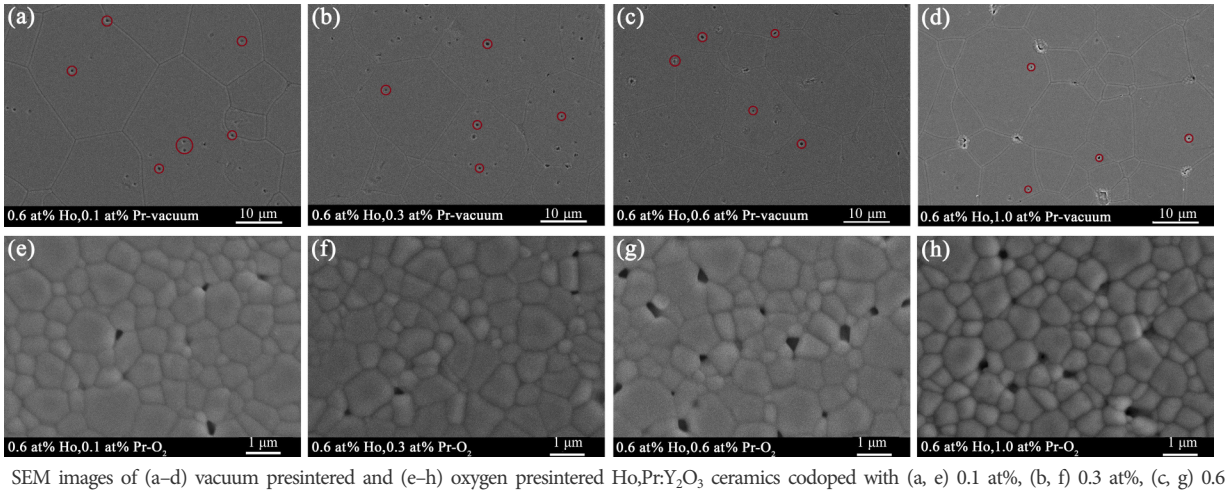

Fig. 3 SEM images of (a–d) vacuum presintered and (e–h) oxygen presintered Ho,Pr:Y_2O_3 ceramics codoped with (a, e) 0.1 at%, (b, f) 0.3 at%, (c, g) 0.6 at%, and (d, h) 1.0 at% Pr at 1520 °C for 7 h.

$O_i^{\cdot\cdot}$ increased accordingly to maintain charge balance. This led to slower grain boundary mobility during the oxygen sintering of the Ho,Pr:Y_2O_3 ceramics, preventing the formation of intragranular pores at the final-stage sintering. Moreover, with increasing Pr incorporation, more pronounced inhibitory effects were observed due to the higher concentrations of $O_i^{\cdot\cdot}$ (Figs. 4(b) and 4(d)). A previous study by the authors [34] revealed that some tetravalent Pr ions remain in Pr-doped Y_2O_3 ceramics under reducing annealing conditions. Therefore, it is reasonable to assume that even under high-temperature vacuum sintering, complete conversion of Pr ions to the trivalent state may not be achieved. This is because the effective ionic radius of Pr^{3+} (0.99 Å) is much larger than that of Y^{3+} (0.90 Å), whereas Pr^{4+} has an ionic radius (0.85 Å) that is more comparable to that of Y^{3+} [41]. The coexistence of these valence states may explain why ceramics with higher Pr doping levels exhibited smaller grain sizes and lower bulk densities during vacuum sintering, as shown in Figs. 4(a) and 4(c).

Defect reactions in Y_2O_3 lattice under Pr oxidation (Eqs. (4) and (5)):

$$Pr^{3+} + \dot{h} \rightarrow Pr^{4+} \quad (4)$$

$$2PrO_2 \xrightarrow{Y_2O_3} 2Pr_Y^{\cdot} + 3O_O + O_i^{\cdot\cdot} \quad (5)$$

To achieve full densification and minimize grain sizes in the final samples, we conducted HIP treatment on the oxygen presintered Ho,Pr:Y_2O_3 ceramics, which had the small average grain sizes and high enough relative densities for self-encapsulation. On the basis of these criteria, the optimal presintering temperatures for $(Ho_{0.006}Pr_xY_{0.994-x})_2O_3$ ceramics were 1460 °C for x = 0.001, 0.003, and 0.006, and 1480 °C for x = 0.01. Under these presintering conditions, the microstructures of Ho,Pr:Y_2O_3 ceramics developed closed pores without abnormal grain growth. The HIP temperature was set at 1450 °C, which is slightly lower than the presintering temperature, to prevent further grain growth. Figures 5(a)–5(d) show SEM images of the Ho,Pr:Y_2O_3 ceramics after HIP. All the oxygen presintered samples exhibited dense and homogeneous microstructures after HIP, with average grain sizes less than 0.8 μm. No inclusions or secondary phases were detected at the grain boundaries.

The HIPed Ho,Pr:Y_2O_3 ceramics were annealed in a reducing 5% H_2/95% Ar atmosphere to increase the proportion of Pr^{3+}. Figure 6(a) presents the XRD patterns of the annealed Ho,Pr:Y_2O_3 ceramics, where all the diffraction peaks were indexed as the cubic Y_2O_3 phase (PDF#74-1828), indicating that both the Ho^{3+} and Pr^{3+} ions had been well incorporated into the Y_2O_3 lattice. Furthermore, there was a slight shift in the diffraction peaks toward lower angles with increasing concentrations of Pr^{3+} (Fig. 6(b)), which could be attributed to the larger ionic radius of Pr^{3+} (0.99 Å) than that of Y^{3+} (0.90 Å), resulting in gradually increasing lattice constants of the Ho,Pr:Y_2O_3 ceramics as the Pr^{3+} concentration increased.

Figure 7(a) shows the absorption spectra of the annealed Ho,Pr:Y_2O_3 ceramics. The main absorption bands at approximately 470, 590, and 1500 nm were assigned to transitions from the ground state $^3H_4$ to the excited states $^1I_6 + {}^3P_{0,1}$, $^1D_2$, and $^3F_3 + {}^3F_4$ of Pr^{3+}, respectively, indicating the obvious generation of

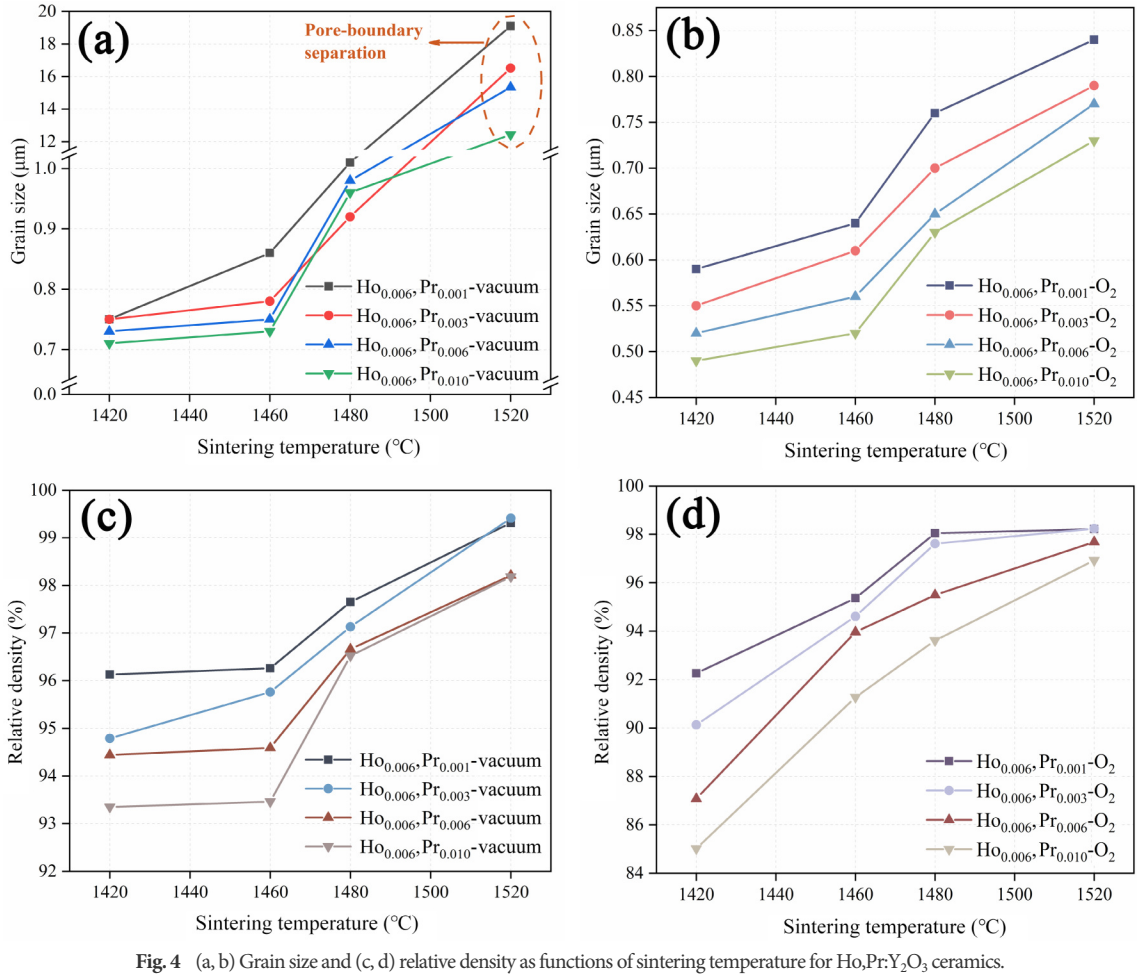

Fig. 4 (a, b) Grain size and (c, d) relative density as functions of sintering temperature for Ho,Pr:Y_2O_3 ceramics.

trivalent Pr ions after reducing atmosphere annealing. Notably, the broad absorption range at 1800–2000 nm related to the Pr^{3+}:$^3H_4$ → $^3F_2$ + $^3H_6$ transitions overlapped with the $^5I_8$ → $^5I_7$ transition of Ho^{3+}, suggesting that Pr^{3+} incorporation may play an effective role in facilitating the deactivation of populations at the Ho^{3+}:$^5I_7$ level. The transmittance spectra of the Ho,Pr:Y_2O_3 ceramics are shown in Fig. 7(b), which exhibit high transmission over both the visible and infrared ranges, with a transmittance of ~81% at 680 nm and ~82% at 1000 nm. These values are in close agreement with the theoretical value (T) of Y_2O_3 crystals calculated via $T = 100\{1 - [(n-1)/(n+1)]^2\}$, where n denotes the refractive index of Y_2O_3 [42]. Figure 7(c) shows photographs of the Ho,Pr:Y_2O_3 ceramics, where the words behind the samples were clearly visible due to their high optical quality. The annealed Ho,Pr:Y_2O_3 ceramics had a yellow–green coloration that became more pronounced with increasing Pr doping. Moreover, larger sizes of Ho,Pr:Y_2O_3 ceramics with high transparency could also be obtained through the oxygen presintering plus HIP method, as shown in Fig. 7(d).

To elucidate the energy transfer processes between the Ho^{3+} and Pr^{3+} ions, the emission spectra of the Ho^{3+}-doped and Ho^{3+}, Pr^{3+} codoped Y_2O_3 ceramics were measured under excitation with a 640 nm laser. The main emission bands in the ranges of 1840–2200 and 2800–3000 nm correspond to the $^5I_7$ → $^5I_8$ and $^5I_6$ → $^5I_7$ transitions of Ho^{3+}, respectively, as shown in Fig. 8.

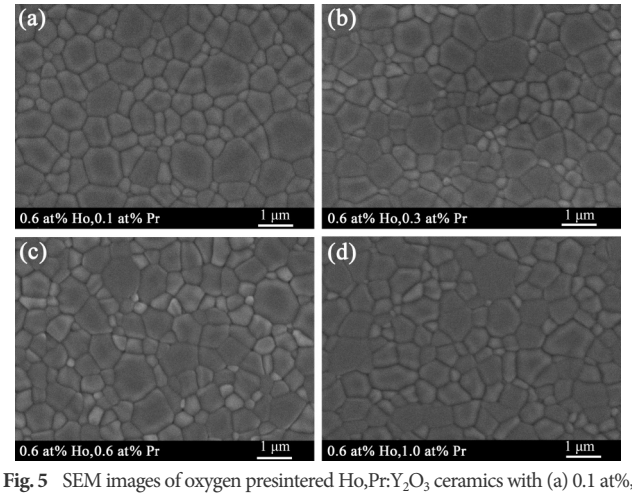

Fig. 5 SEM images of oxygen presintered Ho,Pr:Y_2O_3 ceramics with (a) 0.1 at%, (b) 0.3 at%, (c) 0.6 at%, and (d) 1.0 at% Pr codoping after HIP at 1450 °C.

Figure 8(a) clearly shows that the emission intensity of the Ho^{3+}:$^5I_7$ → $^5I_8$ transition was significantly reduced following Pr^{3+} incorporation. Comparatively, only a slight decrease in the Ho^{3+}:$^5I_6$ → $^5I_7$ emission intensity with low Pr codoping of 0.1 at% was observed, as shown in Fig. 8(b).

These results can be rationalized by the energy level diagram illustrated in Fig. 9 as follows: under 640 nm laser pumping, Ho^{3+} ions can be excited to the $^5F_5$ energy level from the ground state and then fall into the $^5I_6$ energy level by nonradiative relaxation. Subsequently, the particles on the Ho^{3+}:$^5I_6$ level release energy and transit to the $^5I_7$ level instantaneously via the release of photons with a wavelength of 2.9 μm, which ultimately return to the $^5I_8$ level accompanied by 2.1 μm emission. Moreover, two energy transfer upconversion (ETU) processes, including $^5I_7 + {}^5I_7 \rightarrow {}^5I_6 + {}^5I_8$ (ETU 1) and $^5I_6 + {}^5I_6 \rightarrow {}^5F_5 + {}^5I_8$ (ETU 2) between Ho^{3+} ions, operate. The rates of these ETU processes depend mainly on the Ho^{3+} doping concentration [10,11].

After codoping with Pr^{3+} ions, efficient energy transfer (ET 1) from the Ho^{3+}:$^5I_7$ level to the Pr^{3+}:$^3F_2$ level can be achieved because of their similar energy, resulting in a reduction in the number of particles on the upper laser level of Ho^{3+} ions with ~2.1 μm emission. Additionally, an ET 2 process between the energy levels of Ho^{3+}:$^5I_6$ and Pr^{3+}:$^3F_4$ leads to a slight effect on ~2.9 μm emission because of the larger energy gap between them. Nevertheless, significant quenching effects on both ~2.1 and ~2.9 μm emissions from Ho^{3+}-doped Y_2O_3 ceramics can be observed at high doping concentrations of Pr^{3+} ions.

This phenomenon, where the ~2.9 μm emission intensity involving the Ho^{3+}:$^5I_6$ → $^5I_7$ transition decreased with increasing Pr codoping, was also observed in other materials [11,43]. For example, Qiao *et al.* [11] reported that although the emission intensity for the $^5I_6$ → $^5I_7$ transition of Ho,Pr:YAP crystals was weaker than that of Ho:YAP crystals, higher laser efficiency and output power at 3.01 μm were achieved in the former because of the greatly decreased lifetime of the $^5I_7$ level, which suppressed the self-termination effect.

Figures 10(a) and 10(b) show the luminescence decay curves of the $^5I_7$ and $^5I_6$ energy levels of Ho:Y_2O_3 and Ho,Pr:Y_2O_3 ceramics monitored at 2089 and 2843 nm, respectively, which are fitted by a single exponential function. Accordingly, the corresponding relationship between the measured lifetimes and the doping concentrations of Pr is depicted in Fig. 10(c). Codoping with 0.1 at% Pr dramatically decreased the lifetime of the Ho^{3+}:$^5I_7$ level from 11.52 to 3.80 ms, reducing the lifetime ratio ($^5I_7$/$^5I_6$) from

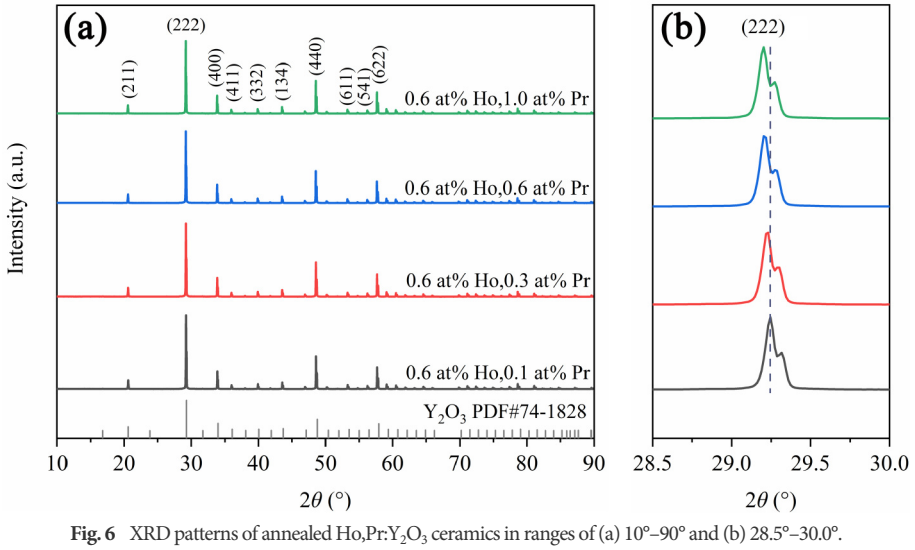

Fig. 6 XRD patterns of annealed Ho,Pr:Y_2O_3 ceramics in ranges of (a) 10°–90° and (b) 28.5°–30.0°.

清華大学出版社 Tsinghua University Press | SciOpen

10.19 to 3.80. These values further decreased to 2.26, 1.74, and finally to 1.53 at the highest Pr doping concentration. The results indicated that the population at the Ho^{3+}:$^5I_7$ level was effectively suppressed through codoping with Pr^{3+}, enhancing the potential

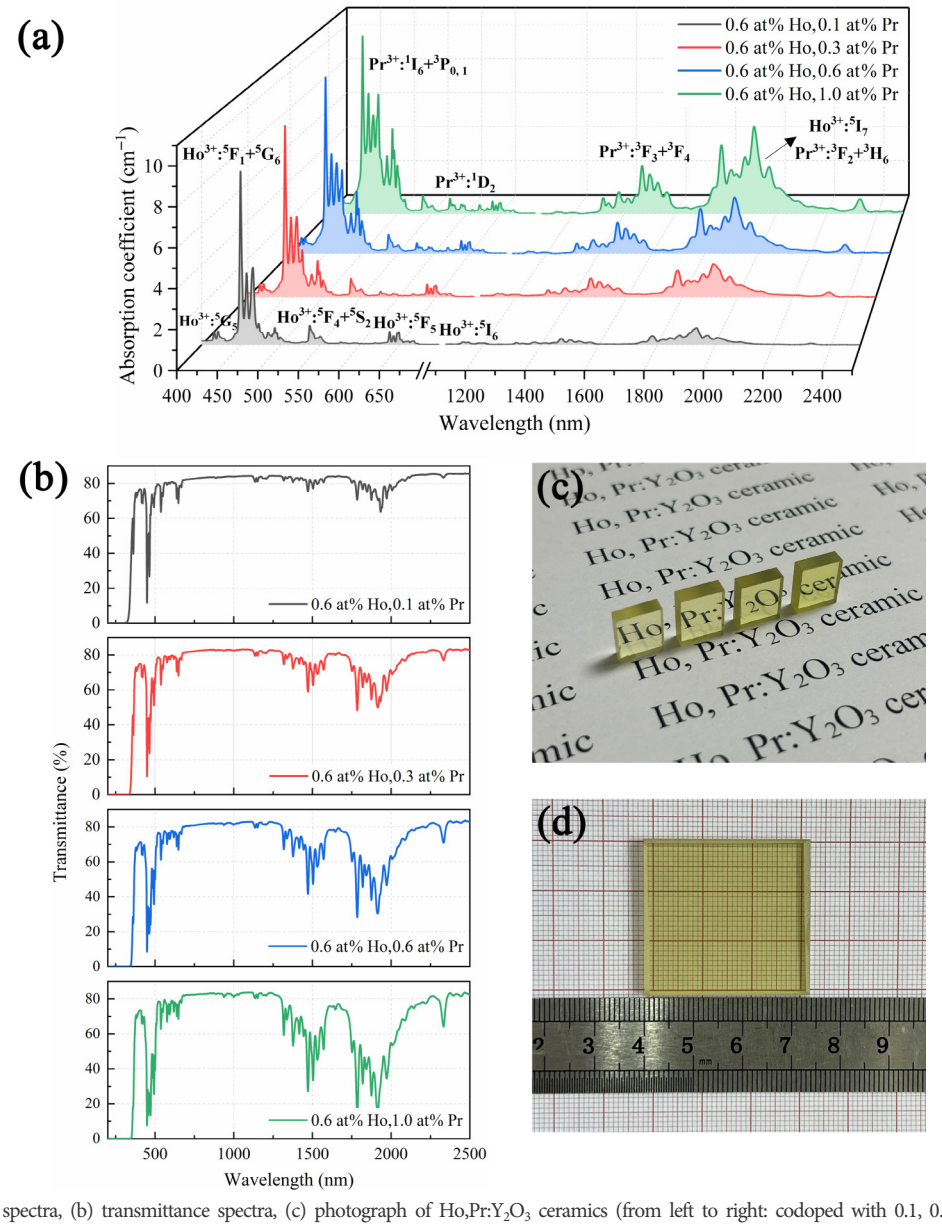

Fig. 7 (a) Absorption spectra, (b) transmittance spectra, (c) photograph of Ho,Pr:Y_2O_3 ceramics (from left to right: codoped with 0.1, 0.3, 0.6, and 1.0 at% Pr, respectively) and (d) Ho,Pr:Y_2O_3 ceramic with a size of approximately 32 mm × 31 mm × 3 mm.

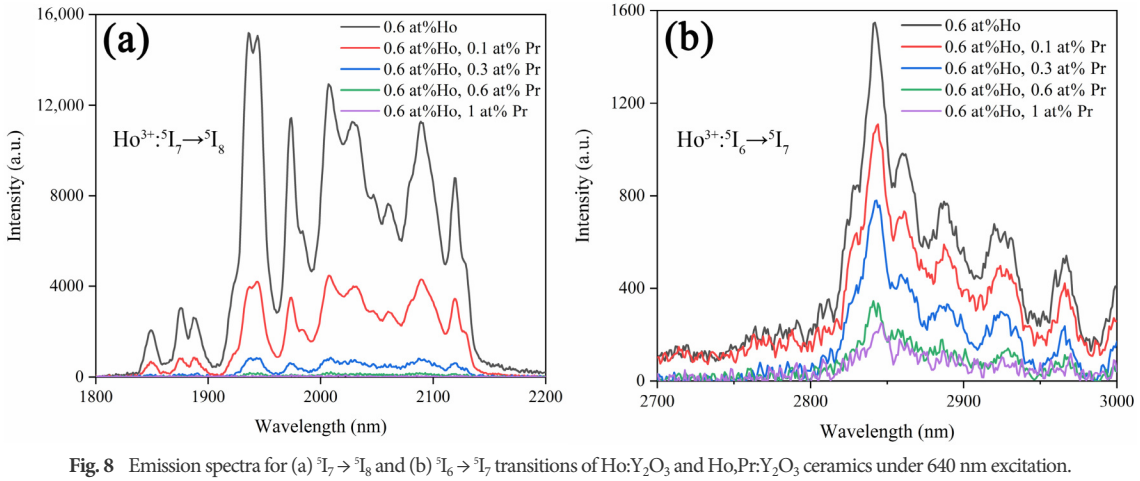

Fig. 8 Emission spectra for (a) $^5I_7 \rightarrow {}^5I_8$ and (b) $^5I_6 \rightarrow {}^5I_7$ transitions of Ho:Y_2O_3 and Ho,Pr:Y_2O_3 ceramics under 640 nm excitation.

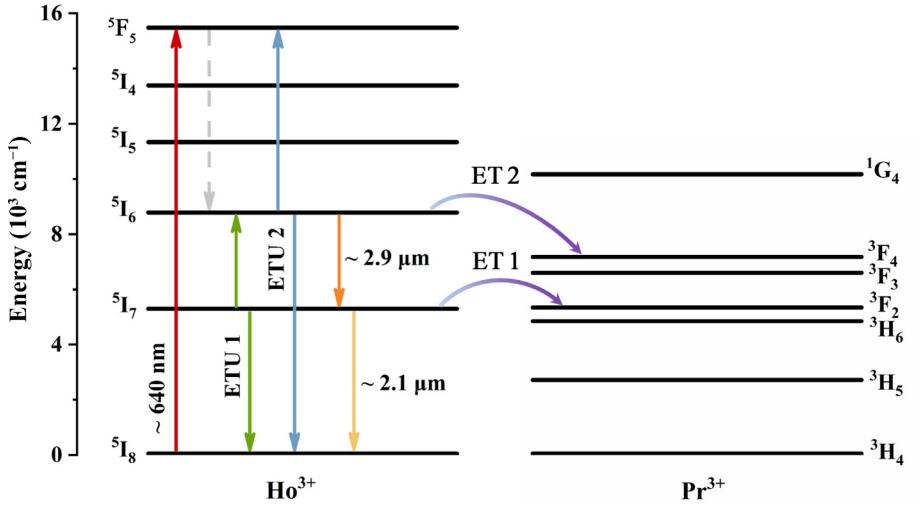

Fig. 9 Schematic diagram of energy transfer process between Ho^{3+} and Pr^{3+} ions in Y_2O_3 ceramics under 640 nm laser excitation.

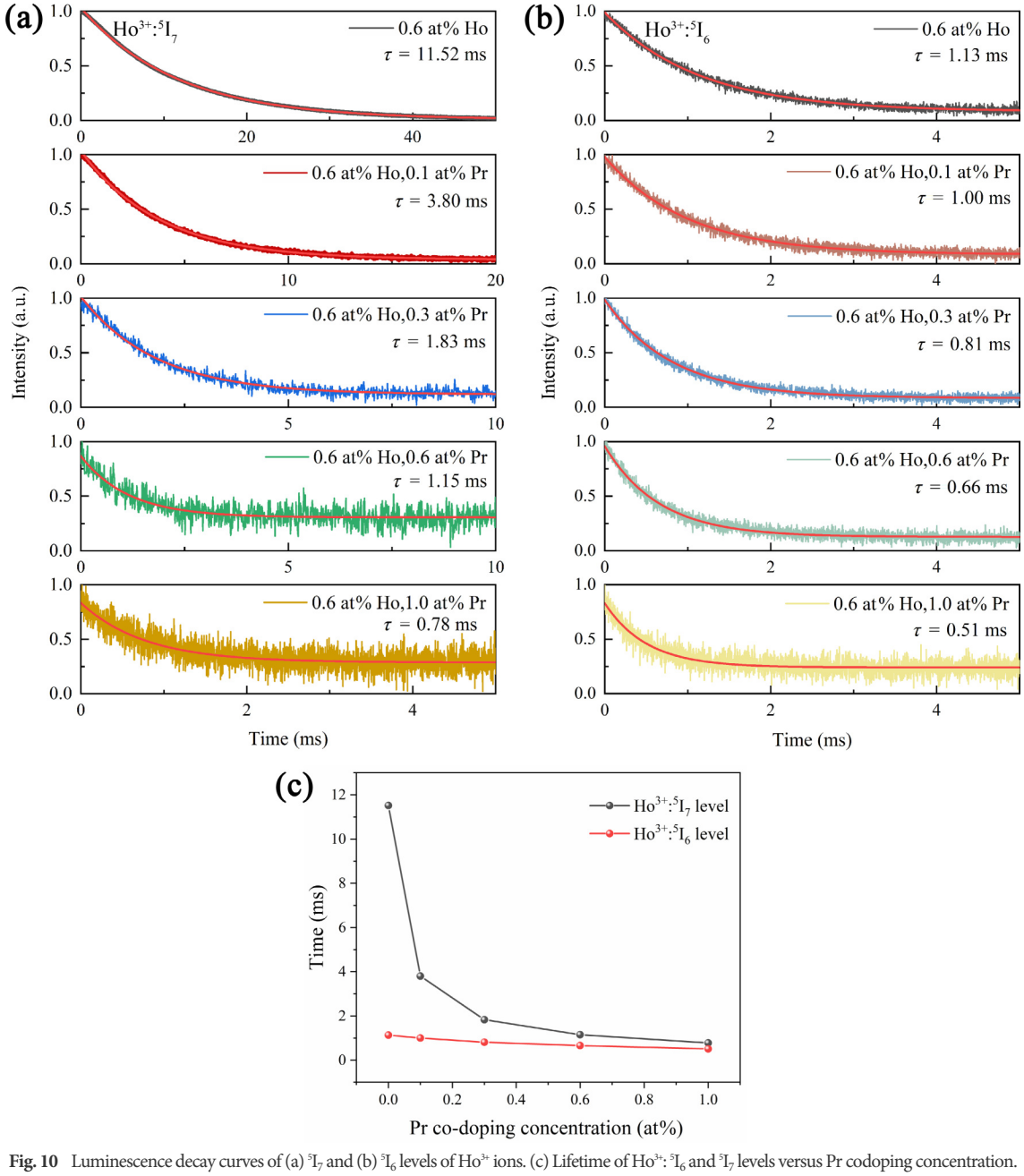

Fig. 10 Luminescence decay curves of (a) $^5I_7$ and (b) $^5I_6$ levels of Ho^{3+} ions. (c) Lifetime of Ho^{3+}: $^5I_6$ and $^5I_7$ levels versus Pr codoping concentration.

for ~2.9 μm laser operation by promoting population inversion in the Ho,Pr:Y_2O_3 ceramics. In contrast, the lifetime of the $^5I_6$ level varied relatively smoothly, indicating the minimal impact of Pr^{3+} ions on the upper laser level ($^5I_6$) of Ho^{3+}.

Furthermore, the energy transfer efficiencies between Ho^{3+} and Pr^{3+} ions were estimated using the formula [11]: $\eta = 1 - \tau_{Ho,Pr}/\tau_{Ho}$, where τ_{Ho} and $\tau_{Ho,Pr}$ represent the lifetimes of the Ho^{3+}:$^5I_6$ and $^5I_7$ levels in Ho^{3+} singly doped and Ho^{3+}, Pr^{3+} codoped Y_2O_3 ceramics, respectively. The calculated values for η were approximately 67.0%, 84.1%, 90.0%, and 93.2% for the ET 1 process with increasing Pr^{3+} concentration, and approximately 11.5%, 28.3%, 41.6%, and 54.9% for the ET 2 process. The higher probability of the ET 1 process compared with the ET 2 process confirmed the strong quenching ability of Pr^{3+} ions toward the populations on the Ho^{3+}:$^5I_7$ level. Notably, the higher codoping concentration of Pr^{3+} could cause an increase in the efficiency of the ET 2 process; thus, a significant quenching of ~2.9 μm emission intensity was observed. In conclusion, the use of a 0.1 at% Pr codoping concentration proved to be advantageous in this study because of its effective depopulation effect on the Ho^{3+}:$^5I_7$ level, without significantly compromising the ~2.9 μm emission intensity and lifetime of the Ho^{3+}:$^5I_6$ level. Furthermore, the optimal doping ratio of Ho^{3+}/Pr^{3+} ions should be optimized for future mid-infrared laser operations on Ho,Pr:Y_2O_3 ceramics, particularly with respect to appropriately increasing the doping concentration of Ho^{3+} ions to facilitate the ETU 1 process [10–12].

4 Conclusions

In conclusion, Ho,Pr:Y_2O_3 transparent ceramics with high optical quality were successfully fabricated through oxygen presintering combined with HIP treatment. The high-temperature oxygen-enriched environment and the oxidization of Pr^{4+} ions promoted the generation of O_i'', thereby the decreased concentration of Y_i''' led to the suppression of grain boundary migration. This allowed for a wider sintering temperature range, preventing pore-boundary separation and facilitating better control of the microstructure during the densification process. The incorporation of Pr^{3+} ions drastically decreased the lifetime of the Ho^{3+}:$^5I_7$ level; thus, the lifetime ratio of $^5I_7/^5I_6$ significantly decreased to attenuate the self-termination effect on the Ho^{3+}:$^5I_6 \rightarrow {}^5I_7$ transition. We believe that the Ho,Pr:Y_2O_3 transparent ceramics can serve as new promising materials for ~2.9 μm mid-infrared laser applications.

Acknowledgements

This research is supported by the National Key R&D Program of China (No. 2022YFB3605800); the National Natural Science Foundation of China (Nos. 62105130, 62075089, 52372010, 52422201, 11654005, and 12234014); the Natural Science Foundation of Shandong Province (No. ZR2023ZD53); the Research Capability Elevation Program of Guangdong Province (No. 2022ZDJS116); the National Science Foundation of Top Talent of SZTU (No. GDRC202302); the Innovation Program for Quantum Science and Technology (No. 2021ZD0303200); the Shanghai Municipal Science and Technology Major Project (Nos. 2019SHZDZX01, 22DZ2229004).

Declaration of competing interest

The authors have no competing interests to declare that are relevant to the content of this article.

References

[1] Ma J, Qin ZP, Xie GQ, *et al.* Review of mid-infrared mode-locked laser sources in the 2.0 μm–3.5 μm spectral region. *Appl Phys Rev* 2019, **6**: 021317.
[2] Yin DL, Wang J, Wang Y, *et al.* Fabrication of Er:Y_2O_3 transparent ceramics for 2.7 μm mid-infrared solid-state lasers. *J Eur Ceram Soc* 2020, **40**: 444–448.
[3] Nie HK, Zhang PX, Zhang BT, *et al.* Diode-end-pumped Ho,Pr:$LiLuF_4$ bulk laser at 2.95 μm. *Opt Lett* 2017, **42**: 699–702.
[4] Quan C, Sun DL, Zhang HL, *et al.* 13-W and 1000-Hz of a 2.7-μm laser on the 968 nm LD side-pumped Er:YAP crystal with concave end-faces. *Opt Express* 2021, **29**: 21655–21663.
[5] Vodopyanov KL, Ganikhanov F, Maffetone JP, *et al.* $ZnGeP_2$ optical parametric oscillator with 38–124-μm tunability. *Opt Lett* 2000, **25**: 841.
[6] Arslanov DD, Spunei M, Mandon J, *et al.* Continuous-wave optical parametric oscillator based infrared spectroscopy for sensitive molecular gas sensing. *Laser Photonics Rev* 2013, **7**: 188–206.
[7] Nie HK, Sun XL, Zhang BT, *et al.* Few-layer $TiSe_2$ as a saturable absorber for nanosecond pulse generation in 295 μm bulk laser. *Opt Lett* 2018, **43**: 3349.
[8] Fan MQ, Li T, Li GQ, *et al.* Passively Q-switched Ho,Pr:$LiLuF_4$ laser with graphitic carbon nitride nanosheet film. *Opt Express* 2017, **25**: 12796–12803.
[9] Liu SD, Nie HK, Zhang BT, *et al.* Continuous-wave-tunable and passively Q-switched 2.9 μm Ho,Pr:$LiLuF_4$ lasers. *Laser Phys Lett* 2019, **16**: 015802.
[10] Ye S, Zhou X, Huang SJ, *et al.* Cascade MIR Ho:YLF laser at 2.1 μm and 2.9 μm. *Opt Lett* 2022, **47**: 5642–5645.
[11] Qiao Y, Sun DL, Zhang HL, *et al.* Thermal, spectroscopy and optimized ~3 μm CW laser properties for Ho,Pr:YAP crystal. *Opt Express* 2023, **31**: 36429.
[12] Nie HK, Xia HP, Shi BN, *et al.* High-efficiency watt-level continuous-wave 2.9 μm Ho,Pr:YLF laser. *Opt Lett* 2018, **43**: 6109–6112.
[13] Nie HK, Shi BN, Xia HP, *et al.* High-repetition-rate kHz electro-optically Q-switched Ho,Pr:YLF 2.9 μm bulk laser. *Opt Express* 2018, **26**: 33671–33677.
[14] Wang YX, Liu JJ, Feng XY, *et al.* ~2.9 μm continuous-wavelength laser operation of fiber-pumped Ho,Pr:CaF_2 single crystals. *Opt Mater* 2023, **135**: 113329.
[15] Zhang HL, Sun DL, Luo JQ, *et al.* Growth, spectroscopy, and laser performance of a radiation-resistant Cr, Yb, Ho,Pr:GYSGG crystal for 2.84μm mid-infrared laser. *J Lumin* 2018, **194**: 636–640.
[16] Qiao Y, Sun DL, Zhang HL, *et al.* Spectroscopy and 3.01 μm laser performance of Ho:YAP oxide crystal pumped by 1150 nm Raman laser. *Opt Laser Technol* 2023, **157**: 108728.
[17] Jackson SD. Single-transverse-mode 2.5-W holmium-doped fluoride fiber laser operating at 2.86 μm. *Opt Lett* 2004, **29**: 334–336.
[18] Crawford S, Hudson DD, Jackson SD. High-power broadly tunable 3-μm fiber laser for the measurement of optical fiber loss. *IEEE Photonics J* 2015, **7**: 1–9.
[19] Walsh BM, McMahon JM, Edwards WC, *et al.* Spectroscopic characterization of Nd:Y_2O_3: Application toward a differential absorption lidar system for remote sensing of ozone. *J Opt Soc Am B* 2002, **19**: 2893.
[20] Ding MM, Li XX, Wang F, *et al.* Power scaling of diode-pumped Er:Y_2O_3 ceramic laser at 2.7 μm. *Appl Phys Express* 2022, **15**: 062004.
[21] Ikesue A, Aung YL. Ceramic laser materials. *Nat Photon* 2008, **2**: 721–727.
[22] Krell A, Hutzler T, Klimke J. Defect strategies for an improved optical quality of transparent ceramics. *Opt Mater* 2014, **38**: 61–74.
[23] Serivalsatit K, Ballato J. Submicrometer grain-sized transparent erbium-doped scandia ceramics. *J Am Ceram Soc* 2010, **93**: 3657–3662.
[24] Chen PL, Chen IW. Grain boundary mobility in Y_2O_3: Defect mechanism and dopant effects. *J Am Ceram Soc* 1996, **79**: 1801–1809.
[25] Zhang C, Wang XL, Liang LX, *et al.* Vacuum sintering of Yb_2O_3 transparent ceramics: Effect of ZrO_2 concentration on structural and optical properties. *J Alloys Compd* 2022, **907**: 164454.
[26] Hou XR, Zhou SM, Li WJ, *et al.* Study on the effect and mechanism

of zirconia on the sinterability of yttria transparent ceramic. *J Eur Ceram Soc* 2010, **30**: 3125–3129.
[27] Ning KJ, Wang J, Ma J, *et al.* Fabrication of laser grade Yb:Y_2O_3 transparent ceramics with ZrO_2 additive through hot isostatic pressing. *Mater Today Commun* 2020, **24**: 101185.
[28] Ikesue A, Kamata K, Yoshida K. Synthesis of transparent Nd-doped HfO_2–Y_2O_3 ceramics using HIP. *J Am Ceram Soc* 1996, **79**: 359–364.
[29] Berard MF, Wilder DR. Cation self-diffusion in polycrystalline Y_2O_3 and Er_2O_3. *J Am Ceram Soc* 1969, **52**: 85–88.
[30] Wang J, Yin DL, Ma J, *et al.* Pump laser induced photodarkening in ZrO_2-doped Yb:Y_2O_3 laser ceramics. *J Eur Ceram Soc* 2019, **39**: 635–640.
[31] Li Q, Wang J, Ma J, *et al.* Fabrication of high-efficiency Yb:Y_2O_3 laser ceramics without photodarkening. *J Am Ceram Soc* 2022, **105**: 3375–3381.
[32] Wang SF, Zhang J, Luo DW, *et al.* Transparent ceramics: Processing, materials and applications. *Prog Solid State Chem* 2013, **41**: 20–54.
[33] Mouzon J, Maitre A, Frisk L, *et al.* Fabrication of transparent yttria by HIP and the glass-encapsulation method. *J Eur Ceram Soc* 2009, **29**: 311–316.
[34] Li Q, Wang Y, Wang J, *et al.* High transparency Pr:Y_2O_3 ceramics: A promising gain medium for red emission solid-state lasers. *J Adv Ceram* 2022, **11**: 874–881.
[35] Yin DL, Wang J, Liu P, *et al.* Fabrication and microstructural characterizations of lasing grade Nd:Y_2O_3 ceramics. *J Am Ceram Soc* 2019, **102**: 7462–7468.
[36] Liu ZY, Ikesue A, Li J. Research progress and prospects of rare-earth doped sesquioxide laser ceramics. *J Eur Ceram Soc* 2021, **41**: 3895–3910.
[37] Frizon V, Bassat JM, Pollet M, *et al.* Tuning the Pr valence state to design high oxygen mobility, redox and transport properties in the CeO_2–ZrO_2–PrO_x phase diagram. *J Phys Chem C* 2019, **123**: 6351–6362.
[38] Lu KL, Ye YC, Han WH, *et al.* Defect elimination to enhance photoluminescence and optical transparency of Pr-doped ceramics for self-calibrated temperature feedback windows. *J Adv Ceram* 2023, **12**: 681–694.
[39] Hu ZW, Cao MQ, Chen HH, *et al.* The role of air annealing on the optical and scintillation properties of Mg co-doped Pr:LuAG transparent ceramics. *Opt Mater* 2017, **72**: 201–207.
[40] Yin DL, Wang J, Liu P, *et al.* Yttria nanopowders with low degree of aggregation by a spray precipitation method. *Ceram Int* 2018, **44**: 20472–20477.
[41] Shannon RD. Revised effective ionic radii and systematic studies of interatomic distances in halides and chalcogenides. *Acta Crystallogr Sect A* 1976, **32**: 751–767.
[42] Nigara Y. Measurement of the optical constants of yttrium oxide. *Jpn J Appl Phys* 1968, **7**: 404.
[43] Qiao Y, Sun DL, Zhang HL, *et al.* Growth, structure and spectroscopy of Ho,Pr:LuYSGG mixed crystals for 2.9 μm emission. *J Lumin* 2023, **253**: 119463.